Journal of Applied Geophysics 152 (2018) 86–99

Contents lists available at ScienceDirect

Journal of Applied Geophysics

journal homepage: www.elsevier.com/locate/jappgeo

Locating scatterers while drilling using seismic noise due to tunnel boring machine

U. Harmankaya [a], A. Kaslilar [a,*], K. Wapenaar [b], D. Draganov [b]

[a] Department of Geophysical Engineering, Faculty of Mines, Istanbul Technical University, 34467 Istanbul, Turkey
[b] Sec. Applied Geophysics and Petrophysics, Dept. of Geoscience & Engineering, Delft University of Technology, The Netherlands

ARTICLE INFO

Article history:
Received 4 June 2017
Received in revised form 18 September 2017
Accepted 16 March 2018
Available online 19 March 2018

Keywords:
Seismic-noise correlation
Tunnel seismic-while-drilling
Body waves
Traveltime inversion
Locating scatterers
Finite-difference modelling

ABSTRACT

Unexpected geological structures can cause safety and economic risks during underground excavation. Therefore, predicting possible geological threats while drilling a tunnel is important for operational safety and for preventing expensive standstills. Subsurface information for tunneling is provided by exploratory wells and by surface geological and geophysical investigations, which are limited by location and resolution, respectively. For detailed information about the structures ahead of the tunnel face, geophysical methods are applied during the tunnel-drilling activity.

We present a method inspired by seismic interferometry and ambient-noise correlation that can be used for detecting scatterers, such as boulders and cavities, ahead of a tunnel while drilling. A similar method has been proposed for active-source seismic data and validated using laboratory and field data. Here, we propose to utilize the seismic noise generated by a Tunnel Boring Machine (TBM), and recorded at the surface. We explain our method at the hand of data from finite-difference modelling of noise-source wave propagation in a medium where scatterers are present. Using the modelled noise records, we apply cross-correlation to obtain correlation gathers. After isolating the scattered arrivals in these gathers, we cross-correlate again and invert for the correlated traveltime to locate scatterers. We show the potential of the method for locating the scatterers while drilling using noise records due to TBM.

1. Introduction

Underground constructions are often conducted in areas with complex geological structures. For tunnel excavations, knowledge of the geological setting and geotechnical parameters are especially crucial. Any sudden changes in geology could cause safety issues for both men and machines, along with any other setback for the drilling project. This is especially important for tunnel boring machines (TBM), due to their limited flexibility towards extreme geological conditions (Petronio and Poletto, 2002). This creates a need for techniques that can detect heterogeneities such as caves, tunnels, fracture zones, *etc*., in front of the TBM before it reaches such areas (Jetschny et al., 2011).

One approach to assess the geological conditions of the drilling site before TBM operation is to obtain a cross-section along the tunnel route by geological observations, borehole drilling, and surface geophysical surveys. However, factors like overburden thickness and topography may limit the potential of these methods to obtain sufficient information on the characteristics of the formation to be drilled by the TBM (Petronio et al., 2007). This creates a problem for the TBM drilling performance and safety, as sudden changes in rock quality can result in damage or loss of equipment.

Due to the limitations of geological mapping, additional methods could also be applied during drilling, such as pilot-tunnel digging and exploratory drilling. While these methods can potentially provide direct information about the rock properties, they cause delays in the tunnel excavation and significantly increase the costs (Petronio and Poletto, 2002). To supplement the limited information obtained from borehole drilling, non-destructive geophysical methods have been developed for predicting interfaces ahead of the tunnel front. These include geoelectrical (Kaus and Boening, 2008; Kopp, 2012; Schaeffer and Mooney, 2016), electromagnetic (Li et al., 2014; Xue et al., 2007) and seismic methods. Due to limited penetration depth of electromagnetic and electrical methods, seismic methods are usually preferred for predictions ahead of the tunnel (Nyugen and Nestorovic, 2016). In-tunnel seismic prediction systems use either an active (explosive, hammer) or passive (TBM) seismic source and an array of receivers located along the tunnel wall and/or on the cutter head of the TBM. An example for the early seismic applications is a horizontal adaptation of the vertical seismic profiling (VSP) technique (Brückl et al., 2001; Sattel et al., 1992), which used reflected energy originating from explosive sources and recorded by sensors located on the tunnel wall. This method was further developed and commercialized into Tunnel Seismic Prediction

* Corresponding author.
E-mail address: kaslilar@itu.edu.tr (A. Kaslilar).

https://doi.org/10.1016/j.jappgeo.2018.03.017
0926-9851/

TSP 202 system (Dickmann and Sander, 1996; Sattel et al., 1996). This method was followed by other seismic-based methods such as True Reflection Underground Seismic Technique (TRUST) (Benecke et al., 2008), the Tunnel Seismic Tomography (TST) (Zhao et al., 2006), and the Tunnel Geological Prediction (TGP) (Jiao et al., 2015). Another technique is the Sonic Softground Probing (SSP), which is a seismic-while-drilling (SWD) method where sources and receivers are located on the cutting wheel of the TBM (Kneib et al., 2000).

All of the methods mentioned above use an active seismic source. A different approach is to use the TBM itself as the source. This methodology is commonly known as tunnel-seismic-while-drilling (TSWD) method (Petronio and Poletto, 2002), where elastic waves generated by the TBM are recorded and processed for the purpose of predicting the geology ahead of the TBM. One advantage of this approach, unlike the active-source methods, is that it does not interrupt the drilling process. Early applications of this method involve cross-correlation of the pilot signal (recorded directly on the TBM) with the data recorded with the sensors along the bored tunnel to provide interpretable seismic data (Brückl et al., 2008; Petronio and Poletto, 2002; Petronio et al., 2007). This method was employed in both hard-rock (Ashida, 2001) and soft-ground (Swinnen et al., 2007) conditions to detect reflections from obstacles ahead of the tunnel. Several studies also used receiver geometries with receivers located outside the tunnel (Hauser, 2001) including with application of seismic interferometry (Poletto and Petronio, 2006). While most of the seismic methods use the traveltimes due to computational efficiency, more recent studies of Musayev et al. (2016a, 2016b) described a method of imaging the geological structure ahead of the TBM by using Full Waveform Inversion (FWI) applied to acoustic waves only.

Here, to locate objects ahead of a TBM, we use a method inspired by seismic interferometry with a TSWD-type survey setting. A method similar to what we propose here was developed for active-source data. It was successfully tested on numerical data and then validated with laboratory and field data sets (Harmankaya et al., 2013; Kaslilar et al., 2013, 2014). The objective of the active-source method was to estimate the location of scatterers by the correlation of isolated scattered waves, extracted from the recorded wavefield *via* filtering (f-k, tau-p) or muting. Here, we discuss the situation where scatterers are located along the tunnel route, and we try to estimate their locations utilizing the seismic-noise records due to an assumed TBM noise source. Noise-source wave propagation is simulated by finite-difference modelling (Thorbecke and Draganov, 2011) in a medium where scatterers are present. Utilizing the simulated noise records, we apply cross-correlation to obtain a correlation gather. Isolation of scattered P-wave arrivals from this correlation gather is followed by another cross-correlation for the inversion of the correlated traveltimes for location purposes.

In the following section, the method and finite-difference modelling is explained of TBM-generated noise in an elastic, dissipation-free medium with one scatterer in it. In the next section, the noise, active-source simulated seismograms, and the correlation gathers for a selected virtual-source location are examined and compared for single- and multiple-scatterer cases. This section is followed by the estimation of location of scatterers. Finally, discussions and conclusions are given.

2. Method and modelling of TBM noise

In this paper, we intend to estimate the location of scatterers (such as boulders, cavities) along a path of a TBM while drilling. Harmankaya et al. (2016) introduced the method we propose and applied it to seismic data, generated by noise sources that simulate a TBM, to locate scatterers ahead of the TBM. In this section, we first explain the noise correlation and how non-physical (*e.g.*, nP) arrivals are retrieved. We then show modelling results of noise sources due to TBM in a model of a simple subsurface containing only one scatterer.

The cross-correlation of records that are generated by sources of equal power located on a surface enclosing the receivers enables the extraction of Green's functions (Snieder et al., 2008; Wapenaar et al., 2010). In our experiment with scatterer(s) in a medium, the receivers are at the surface and are not surrounded by the sources. In such a case, non-physical (spurious) arrivals will emerge, particularly for the cross terms between scattered waves. Such retrieved arrivals are called non-physical as they are not part of the Green's function. A detailed discussion about non-physical arrivals due to scatterers is given in Snieder et al. (2008) and Snieder and Fleury (2010). In our method, we specifically use these non-physical arrivals due to scattered waves and estimate the location of scatterer(s). Therefore, for our method suppressing the non-physical arrivals in the retrieved Green's function is not required, as they are used in an opportune way.

Let us consider receivers r_i at the surface (i: receiver index, $i = 1,2,\ldots n_r$; n_r: number of receivers) where one of the receivers is arbitrarily selected to be converted into a virtual source (vs) – r_{vs}. When applying seismic interferometry by cross-correlation to the recordings at the receivers, the retrieval of non-physical arrivals between the scatterer and the receivers can be explained by considering Fig. 1. In the figure, only wave propagation from the source(s) to the receivers *via* the scatterer is illustrated for explanatory purposes. For the scattered waves, the traveltime from the source s to the virtual source vs is represented by $t_{vs} = t_s + t_1$, and to one of the receivers by $t_i = t_s + t_2$ (Fig. 1a). The traveltime between the source and scatterer is given by t_s, while t_1 and t_2 are the travel times between the scatterer and receivers, *i.e.*, r_{vs} and r_i, respectively. Note that the source can be at any position along the surface or in the subsurface (Fig. 1a, explosions).

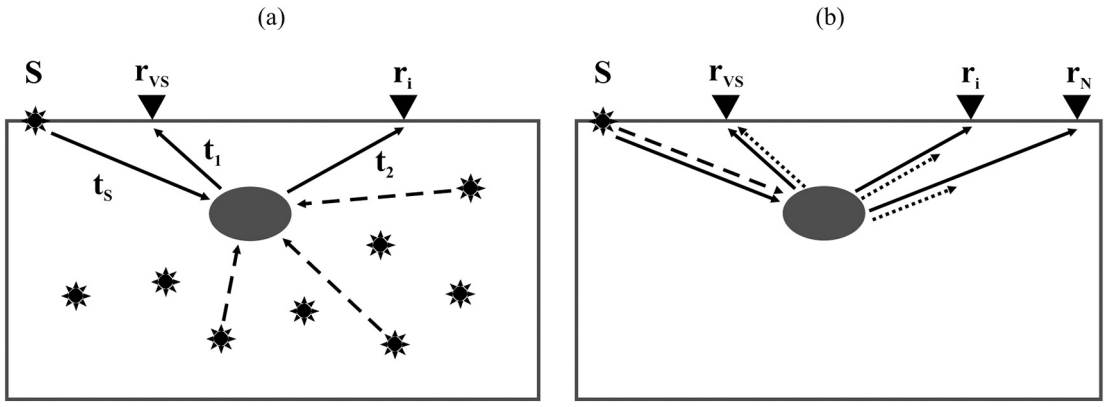

Fig. 1. (a) Geometry of sources (explosions) and receivers (triangles) and travel paths from the source to the receivers *via* a scatterer. r_{vs} and r_i represent the locations of a virtual source and another receiver used for acquisition, respectively. The dashed lines represent paths from sources in the subsurface to the scatterer. (b) Physical travel paths between the scatterer and the receivers r_{vs}, r_i, and r_N (solid lines) and eliminated travel paths (dashed and dotted lines) after correlation.

Since the cross-correlation results in the difference of arrival times of the waves with respect to the trace at the *vs* location, the common travel path from the source to the scatterer (t_s) is eliminated (Fig. 1b dashed line). Also the travel path from scatterer to *vs* location, with the travel time t_1, is eliminated from all available travel paths between the scatterer and the receivers (Fig. 1b, dotted paths). This results in the retrieval of non-physical arrivals, *i.e.*, the traveltimes obtained by cross-correlation do not correspond to times of a physical wave that propagates between *vs* and the receivers *via* the scatterer (Meles and Curtis, 2013; Snieder and Fleury, 2010; Snieder et al., 2006, 2008). As can be observed in Fig. 1b, the arrival times from the scatterer to the receivers do not depend on the source location (Fig. 1a, explosions), and are always constant (stationary with respect to the different source locations) as long as the location of the scatterer does not change.

The response to a bandlimited noise source $S(t) = N(t)$ at position x_s observed by one of the receivers at position x_i can be written as

$$u(x_i, x_s, t) = G(x_i, x_s, t) * N(t) \qquad i = 1, 2, \ldots, n_r, \tag{1}$$

and, similarly, the response observed by the receiver at the selected virtual-source position is

$$u(x_{vs}, x_s, t) = G(x_{vs}, x_s, t) * N(t). \tag{2}$$

In the above equations, $*$ represents temporal convolution, t is time and G is the Green's function from the source x_s to the receivers at x_i and x_{vs}. The cross-correlation of the responses at the receivers (Eq. 1) with the response at the *vs* location (Eq. 2) is then

$$G(x_i, x_{vs}, t) * S_N(t) = u(x_i, x_s, t) * u(x_{vs}, x_s, -t) = u(x_i, x_s, t) \otimes u(x_{vs}, x_s, t), \tag{3}$$

where $\otimes$ denotes correlation, $S_N(t)$ is the autocorrelation of noise $N(t)$, and $G(x_i, x_{vs}, t)$ is the response between the virtual source and the receivers.

In our case the receivers are not surrounded by sources, so the cross-correlation will not converge to the correct Green's function and its time-reversed version, but the non-physical arrival of the Green's function, as described by Eq. 3, will stack coherently for any source distribution.

To explain and demonstrate the extraction of scattered waves from noise records, we consider a simple model where one scatterer is present in a homogeneous half space (Fig. 2). We perform 2D finite-difference modelling (Thorbecke and Draganov, 2011) and record the noise at the surface during a short advance of a TBM. In real TBM experiments, the noise (vibrations) are generated by the cutting blades, the rotating wheel of the TBM, and by the rock failures during drilling, as explained in detail by Petronio and Poletto (2002). The composed noise generated by these discrete sources is recorded at far distances with high level of energy (Petronio and Poletto, 2002). In our modelling, to simulate these discrete sources we define an area in the model (grey rectangle in Fig. 2), which represents the TBM cutter head. Within this area 16 noise sources are generated at random positions (see zoomed image in the right of Fig. 2). Each of the 16 sources has random activation and duration time (Fig. 3). The individual noise sources are band limited with maximum frequency of 150 Hz (Brückl et al., 2010; Petronio and Poletto, 2002). We consider the sources to be uncorrelated. The average duration of each source signal is 50 s; the total duration of the modelling is 120 s, which is considered as the operation time of the TBM, and the temporal sampling of seismograms is 1 ms.

The TBM cutter head, represented by the grey rectangular area in Fig. 2, is at a depth of 18 m, having 1 m width and 6 m height. The background velocities are set to 600 m/s (Vp) and 350 m/s (*Vs*), the density as $\rho = 2200$ kg/m^3, representing very soft-ground tunneling conditions. The scatterer is located ahead of the TBM path to represent a cavity that could threaten the tunneling operations. As the scatterer represents a subsurface cavity, it has the velocity and density parameters of air (Vp = 340 m/s, $\rho = 1.29$ kg/m^3). The modelled wavefields are recorded by 131 receivers located at the surface and spaced at 1 m. Considering the background P- and S-wave velocities of 600 m/s (V_P) and 350 m/s (V_S) and the dominant frequency around 60 Hz, the dominant wavelengths would be $\lambda_P = 10$ m and $\lambda_S = 5.8$ m for the P- and S-waves, respectively, which are comparable to the size of the scatterer.

Fig. 4a and b show the recorded wavefield and the trace at receiver 20, respectively, for the noise-source modelling. This wavefield, but also all other wavefields from this study, is the particle-velocity field. Here, we can see that the highest amplitudes are recorded with the receivers located directly above the noise sources (Fig. 4a, arrow). In its raw form, effects from the scatterers are not visually interpretable in the recorded wavefield. As can be observed in Fig. 3, the first noise source is activated after nearly 15 s (dashed line) from the start of the record, hence the quiet period at the start of the noise record in Fig. 4a and b. To obtain the correlated wavefield, we arbitrarily select a trace from the noise record (Fig. 4b) as a *vs*, and cross-correlate all the traces from Fig. 4a with the trace at the *vs* location to obtain Fig. 4c. For both the selected *vs* trace and the other traces, the 120-s-long record is partitioned into 10-s-long segments. These segments are then correlated and the results are summed to obtain the final wavefield shown in Fig. 4c. As the correlated segments are 10-s long, the correlations are actually ranging from −10 s to +10 s, but we show the correlation results only from −0.25 s to 0.25 s to be able to observe the relevant arrivals more clearly.

As stated before, the cross-correlation gives the difference of the arrival times of the waves with respect to the trace at the *vs* location. The correlation of the trace at the *vs* location with itself results in an arrival time $t = 0$ s (Fig. 4c grey arrow), whereas the other arrivals are shifted with respect to the *vs* (Fig. 4c). Although uninterpretable, the noise records at the receivers (Fig. 4a) contain both direct and scattered waves. Hence, the cross-correlation of these records and their summation will result in the retrieval of both physical and non-physical arrivals

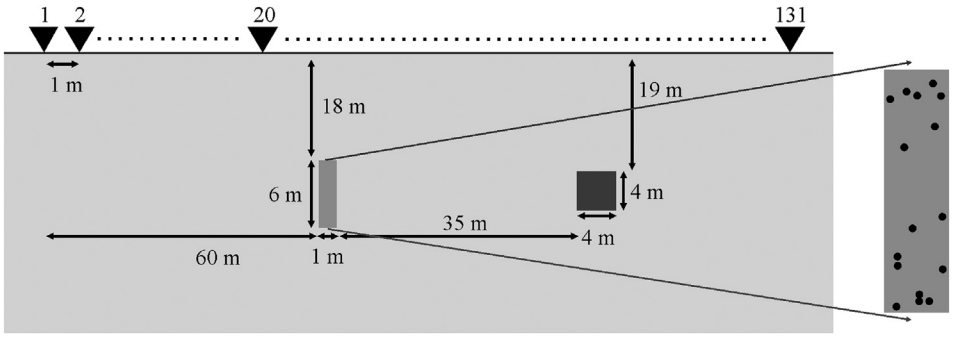

Fig. 2. Schematic view of a simple model consisting of a homogeneous half space containing one scatterer (black square) with noise-source area representing a TBM cutter head (grey rectangle) and receivers (triangles). A random distribution of noise sources is shown at the right side of the figure.

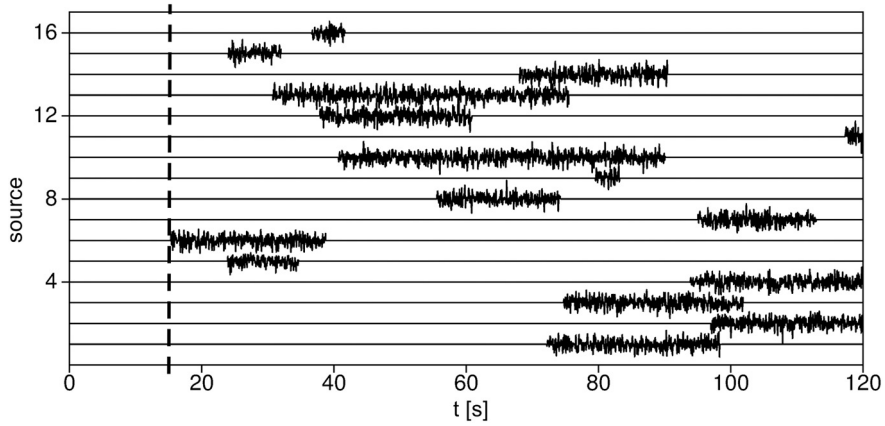

Fig. 3. Noise signals that were used in the noise-source modelling of the TBM. Each noise source has a randomly generated activation time and signal duration. Dashed line marks the starting time of the first source signal.

(Snieder et al., 2008). For example, correlation of a direct arrival at the *vs* location with its free-surface multiple recorded at another receiver location after being scattered by the scatterer will result in the retrieval of a physical scattered arrival. In a similar way, correlation of a scattered arrival at the *vs* location with its free-surface multiple at another receiver will result in the retrieval of the same physical scattered arrival as above. On the other hand, correlation of two scattered arrivals from the subsurface noise source through the scatterer to the receiver at *vs* and at another receiver (like in Fig. 1a) will retrieve non-physical scattered arrivals (Snieder and Fleury, 2010; Snieder et al., 2008) independent of subsurface-source position, as explained above. After retrieval of a *vs* at the surface, we can apply the method of Harmankaya et al. (2013) for the estimation of the scatterer's location. This method requires the extraction of the non-physical scattered waves between the scatterer and the receivers.

In case of a noise record, or a seismic record from a complex area, it may be difficult to decide a proper virtual-source location that extracts the non-physical arrivals between the scatterer and the receivers in a single cross-correlation step. This may happen due to the signal being undetectable or due to interference with other arrivals in such records. Therefore, depending on the choice of the virtual-source location, the first correlation may not provide the arrivals between the scatterer and receivers. In other words, the first correlation may not eliminate the complete path between the source and the scatterer. In such a case, a second cross-correlation step becomes necessary. An example for such a case is given in Fig. 5a, where direct arrivals, from the source to the receivers, and scattered arrivals, from the source to the receivers *via* the scatterer, are present (see Table 1 for explanations). When $r_{vs'}$ is chosen as the virtual-source location, the dotted path in Fig. 5b, which is equal to the path from the source to $r_{vs'}$, are eliminated after cross-correlation from the path from the source to the scatterer, and one is left with the travel paths given in Fig. 5c, where a section of the path between the source and scatterer has remained. As for application of our method the non-physical travel paths between the scatterer and the receivers are required, a second correlation becomes necessary to eliminate the remaining path between the source and the scatterer (Fig. 5c, thick arrow). Therefore, we select again a virtual source location, $r_{vs''}$, and apply a second cross-correlation to the records represented by the travel paths in Fig. 5c. By the second cross-correlation, the dotted paths in Fig. 5d are eliminated and the non-physical arrivals between the scatterer and receivers are obtained. The traveltime differences, *i.e.*, cross-correlation times, obtained after the first and the second cross-correlation steps are given in Fig. 5b and d (see Table 1 for explanations).

Therefore, after the noise correlation and summation (Fig. 4c), we select the non-physical scattered wavefield (nP_{sc} or nS_{sc} in Fig. 4c)

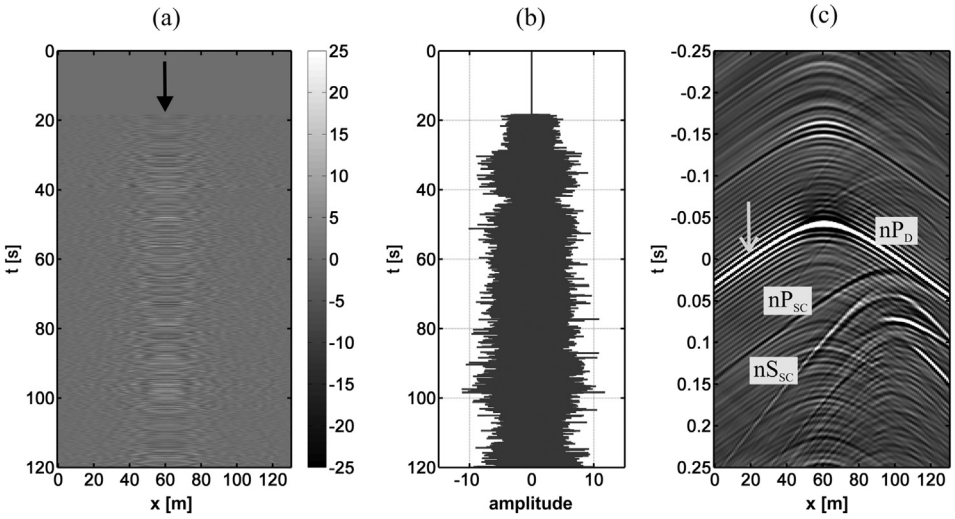

Fig. 4. (a) Recorded wavefield from the noise sources for the model in Fig. 2. (b) The trace recorded at receiver 20 (virtual source). (c) Correlated and summed panel for virtual source 20 (*vs*20). nP_D is a non-physical P-wave arrival from the correlation of the direct arrivals from the noise sources. nP_{SC} and nS_{SC} are non-physical arrivals due to the scattered P- and S-wave arrivals, respectively.

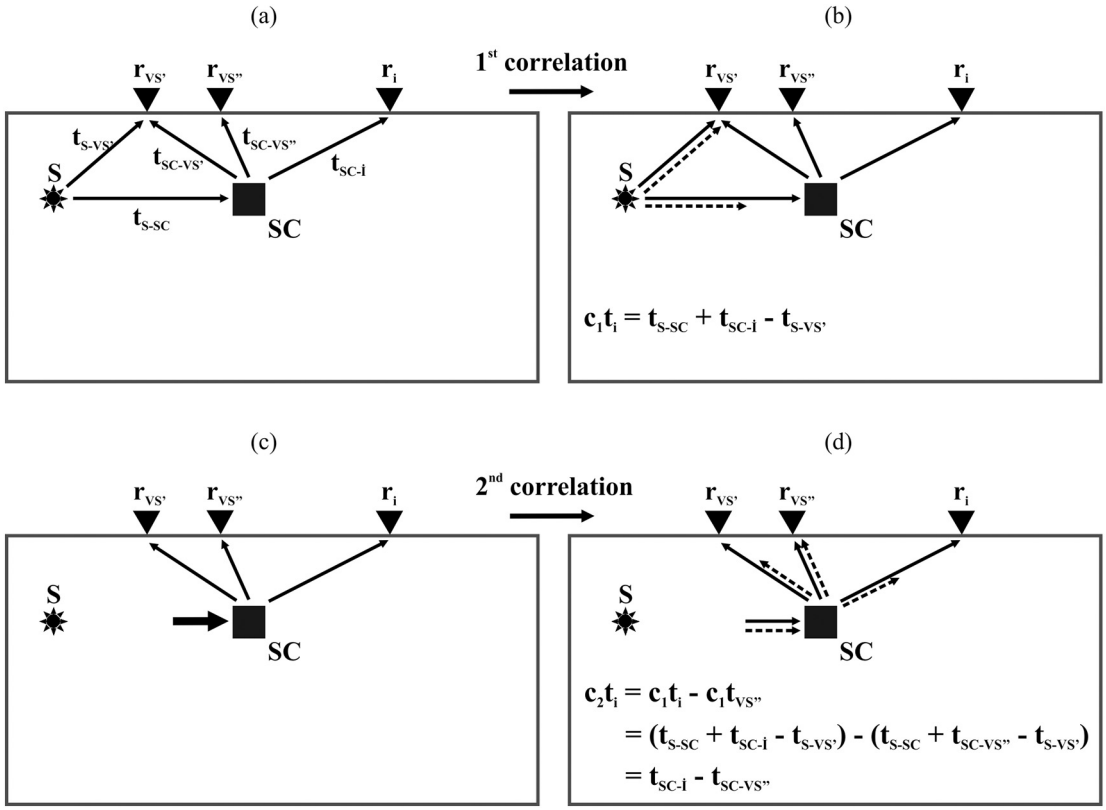

Fig. 5. (a) Actual travel paths between source, scatterer and receivers. (b) Elimination of travel paths with the first correlation for a virtual source at $r_{VS'}$. (c) Remaining travel paths after the first correlation. (d) Elimination of travel paths with the second correlation for a virtual source at $r_{VS''}$. Dashed lines represent the eliminated travel paths in each correlation.

from the noise correlated record by muting or filtering and apply cross-correlation again to the traces of the selected scattered waves. In this way the remaining paths between the source and the scatterer will be eliminated, and we will have the non-physical arrival times between the scatterer and the receivers. In Fig. 6a and b we show the scattered field nP_{sc} obtained from Fig. 4c by muting and its cross-correlation with the field at *vs* trace 30 (this is the trace at x = 29 m). The arrivals given in Fig. 6b are the ones that are used in the estimation of the location of the scatterer. The estimation procedure will be explained in Section 4.

In this section, we explained the noise correlation and have shown the modelling and the correlation procedures for a simple example. In the following section, we consider three scatterers in the homogeneous half space and model wave propagation with all scatterers present in the medium simultaneously. We discuss the scattered arrivals in detail and show that the records obtained by random discrete noise sources can be obtained from a single active source placed in the middle of the grey rectangular area in Fig. 2.

Table 1
Explanation of abbreviations used in Fig. 5.

S	Actual source
SC	Scatterer
r_i	Receiver *i*
$r_{VS'}$	Virtual source for first correlation
$r_{VS''}$	Virtual source for second correlation
$t_{S-VS'}$	Traveltime from source to virtual source for first correlation
t_{S-SC}	Traveltime from source to scatterer.
$t_{SC-VS'}$	Traveltime from scatterer to virtual source for first correlation
$t_{SC-VS''}$	Traveltime from scatterer to virtual source for second correlation
t_{SC-i}	Traveltime from scatterer to receiver i.
c_1t_i	Cross-correlation traveltime to receiver *i* after first correlation
$c_1t_{VS''}$	Traveltime to second virtual source after first correlation
c_2t_i	Non-physical scattered-wave traveltime to receiver *i* after second correlation

3. Modelling with multiple scatterers

In this section, we consider a model where more than one scatterer is present. To simulate the TBM noise, we consider modelling parameters similar to those in the previous section. The seismic-noise modelling is conducted with noise sources located inside a rectangular area representing the cutter head of the TBM. While the model in the previous section had only one scatterer, this model (Fig. 7) contains three scatterers (*sc1*, *sc2*, and *sc3*) with varying depth and distances to the TBM. The medium parameters (except for the scatterers' geometry), source parameters, and receiver locations are the same as for the previous model.

The correlated wavefield is obtained in the same manner as discussed in the single-scatterer example by selecting the *vs* at receiver 20 (*vs*20), see Fig. 8a. The noise recording at *vs*20 is cross-correlated with the recordings at the other traces (Fig. 8b) and summed over the 10-s windows. The retrieved panels are only shown between −0.2 s to 0.3 s to better observe the arrivals and match the record length to subsequent active-source modelling cases. It should be noted that the duration of the noise record is selected as 120 s to provide enough stacking to improve the signal-to-noise ratio in the retrieved result. However, it was also possible to obtain a similar retrieved result from only 15-s-long noise record (Fig. 9b). Due to the larger number of stacks for the 120-s recording, the retrieved non-physical scattered arrivals are enhanced (see dashed circles in Fig. 9, for example) in the retrieved result (Fig. 9a).

To get a better idea about the arrivals from the retrieval process, we also modelled an active transient source located at the centre of the grey rectangle in Fig. 7. Fig. 8c and d show the recorded wavefield from the active source and the correlation result with a trace at position of *vs*20, respectively. Comparing Fig. 8b and d, apart from the difference in frequency content, most of the significant arrivals can be clearly observed at the same arrival times in both correlation gathers. The

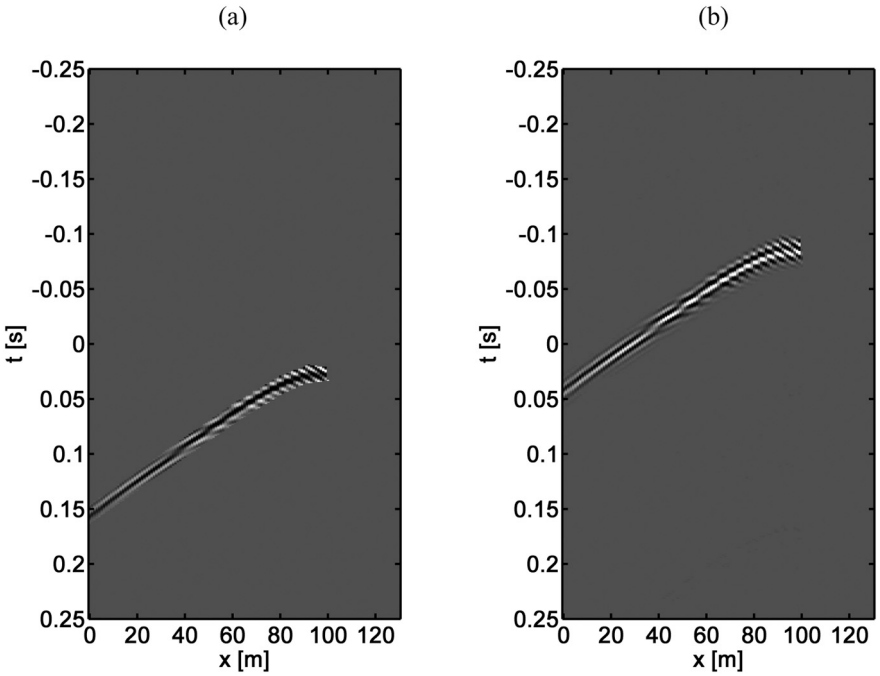

Fig. 6. (a) Isolated retrieved non-physical P-wave scattered arrivals (nP_{SC} in Fig. 4c). (b) Cross-correlation of the scattered P-wave arrivals given in (a) with the trace at *vs*30 (29 m).

frequency difference between these results is due to difference in the frequency contents of the transient- and noise-source signals, as can be seen from the amplitude spectra in Fig. 10. As our aim is to show that both transient- and noise-source signals give similar correlation results, *i.e.*, that the retrieved arrival times of the events of interest are practically the same, there is no need for the amplitude frequency spectra of the source signals to be identical. Comparisons of the two pairs of retrieved traces from active- and noise-source modelling are given in Fig. 11. Fig. 11a shows the correlated trace 20 from the active- and noise-source modelling, which is relatively distant from the scatterers. Trace 20 is also the selected virtual source for the retrieval in this case, thus the highest-amplitude arrivals (the direct non-physical P (nP_D)) are observed at zero lag ($t = 0$ s). For trace 60 in Fig. 11b, we can see that the nP_D arrival is shifted by nearly 45 ms from zero lag, and, compared to trace 20, the nP_{SC} (scattered P) and nS_{SC} (scattered S) arrivals are grouped more closely as trace 60 is nearer to the scatterers. We can also see that the high-frequency content is more significant in the noise-source modelling, which is also evident from the frequency contents of the source signals in Fig. 10. It should also be noted that pressure-type sources are used for both active- and noise-source modelling, therefore the direct S-waves in Fig. 8b–d are not present.

Based on the correlation panels, it can be said that the active- and noise-source results produce similar physical and/or non-physical arrivals. Therefore, in the following tests in this section we make use of active-source modelling as a proxy to noise-source modelling since the former is computationally cheaper, due to the fact that active-source cases are only modelled for a duration of 0.5 s, whereas noise-source cases are modelled for 120 s. However, as the focus of this study is to use TBM noise as a source to estimate the locations of scatterers, in the next section we use the noise-source modelling to estimate the location of scatterers.

As can be seen in Fig. 8b, the scattered wavefield is quite complicated due to the presence of several scatterers. Here, the scattered wavefield is composed of primary (source to receiver *via* single scatterer) P- and S-wave scattering, but also of the multiple scattering (source to receiver *via* several scatterers) due to interaction between the scatterers. For further examination, each scatterer is also modelled individually with an active source (Fig. 12). The modelling results for each scatterer are given in Fig. 12a–c, while their superposition is given in Fig. 12d. Due to the nature of the 2D modelling, the slope of the scattered arrivals only depends on the depth of the scatterer for a given background velocity. As observed in Fig. 12a–c, the slope of the

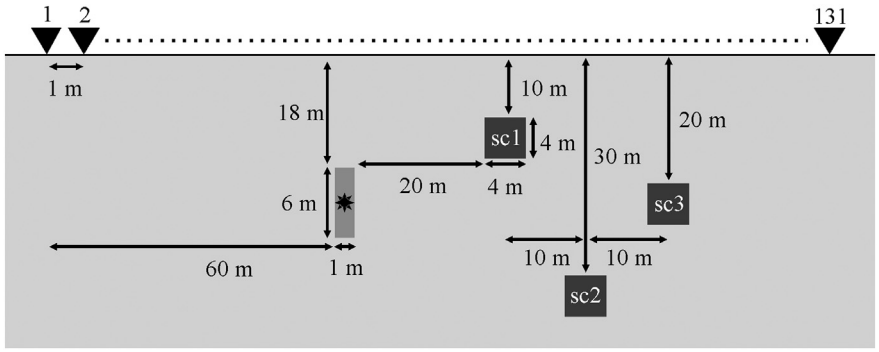

Fig. 7. Schematic view of the model consisting of a homogeneous half space containing three scatterers (black squares) with noise-source area representing a TBM cutter head (grey rectangle) and receivers (triangles). The star inside the grey rectangle indicates the location of a deterministic source for active-source modelling.

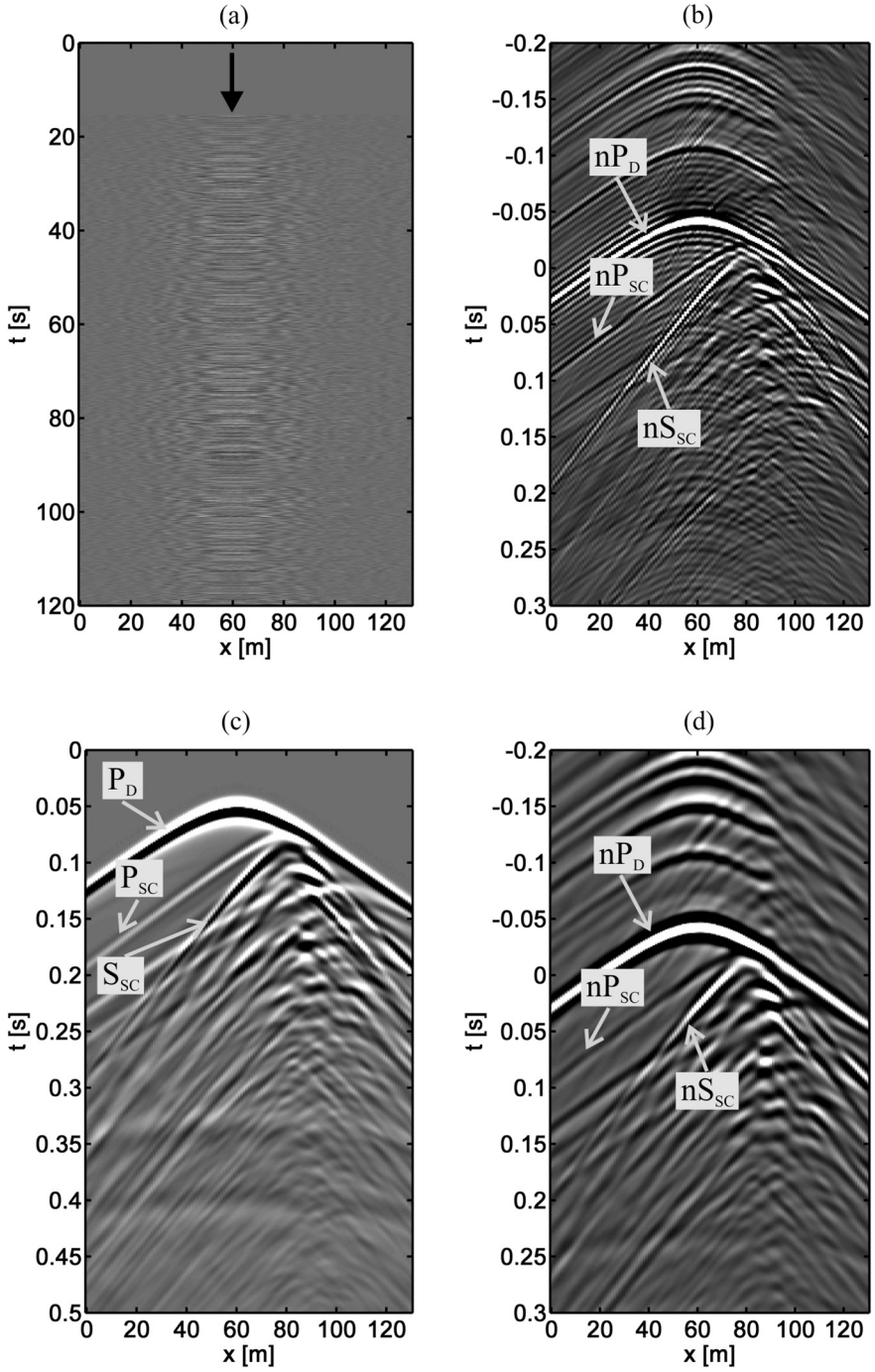

Fig. 8. (a) Recorded wavefield from the noise sources for the model given in Fig. 7. (b) Correlated and summed panel for *vs*20. (c) Recorded wavefield from an active source located at the centre of the noise-source area in Fig. 7 (star). P_D, P_{SC} and S_{SC} are direct P-, scattered P- and scattered S-wave, respectively. (d) Correlated active-source wavefield for *vs*20. nP_D is a non-physical P-wave arrival from the correlation of the direct arrivals. nP_{SC} and nS_{SC} are non-physical arrivals due to the scattered P- and S-wave arrivals from the scatterer 1.

scattered arrivals from *sc1* is steeper compared to the slope from *sc2* and *sc3*. The correlation procedure is the same as the one used for the noise-source case, except that here we correlate only one panel. The same virtual source is chosen for comparison purposes. Fig. 13a–c show the correlation results using recorded wavefields obtained from isolated modelling of the scatterers, while Fig. 13d shows the superposition of these three results. The superposition of single-scatterer cases gives the same result as for the case of three-scatterers modelling, except that events due to the multiple scattering between the three scatterers are not present and that P_D is stronger. This can be seen from the comparison of Fig. 14a and b. Fig. 14c shows the difference between these two results, where the primary scattering is removed as expected, leaving the clearly observable multiple scattering and P_D.

4. Estimating the locations of the scatterers

The success of the method that we use to estimate the location of a scatterer depends on whether we can clearly interpret the scattered arrivals on the correlation panels, or at least pick out a flank and the

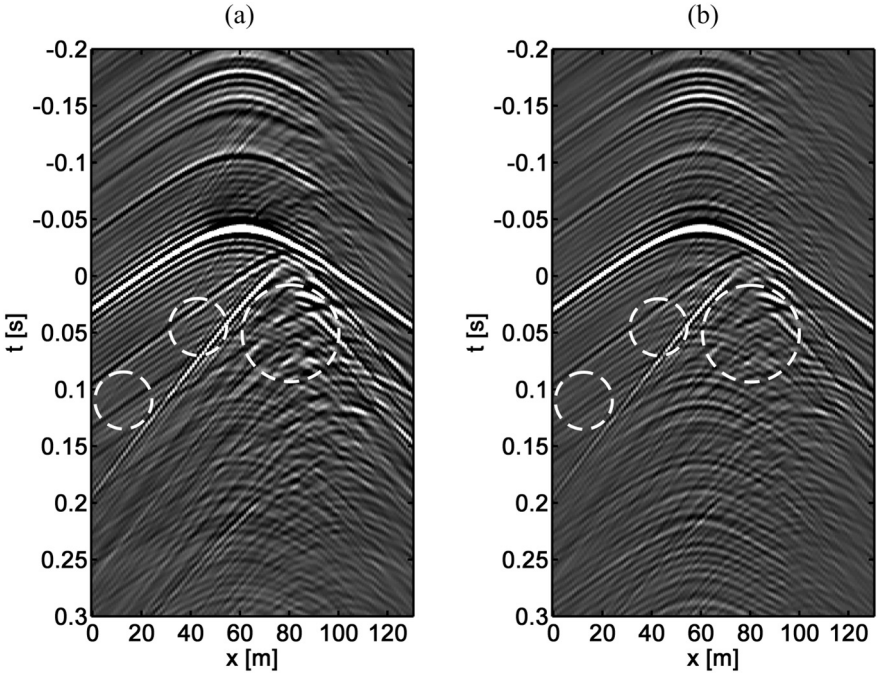

Fig. 9. Retrieved result from (a) 120 s and (b) 15 s noise-record length. Note that the signal-to-noise ratio for the nP_{SC} and nS_{SC} in (a) is higher, as can be observed in arrivals marked by the white circles.

apex of the scattered arrivals. Examples of such arrivals are labelled on the correlation results from the single-scatterer modelling (Fig. 13a–c). However, the presence of multiple scatterers reduces the possibility of selecting a clear scattered arrival from some of the scatterers. From the panel in Fig. 15a (repeated from Fig. 8b), it can be seen that scattered arrivals due to *sc1* (leftmost) can be easily selected. While it was also possible to select arrivals from *sc3* (rightmost), most of the arrivals from *sc2* (middle) are masked by various other arrivals. Although some arrivals from *sc2* are interpretable on the correlation result, due to the interference with other arrivals it is very difficult to isolate the former from the latter. Even for the superposition of the seismograms from single-scatterer modelling (Fig. 12d), the scattering due to *sc2* becomes almost indistinguishable.

To use the method given in Harmankaya et al. (2013), we isolate the interpretable nP-wave arrivals from *sc1* and *sc3* (Fig. 15b–c) from the correlation panel (Fig. 15a). To apply the method, we need the travel paths between the scatterer and the receivers. To obtain this, we choose *vs* locations and apply a second cross-correlation process to all the traces with the trace at the *vs* location, but now using only the wavefields in Fig. 15b and c. In this way, the dependence of the travel-time differences on the TBM location in the correlations is eliminated, and non-physical scattered arrivals are retrieved, which depend only on the scatterer location. As the location of the scatterer does not change, the arrival times from the scatterer to the receivers are always constant (stationary), irrespective of the path to the scatterer (Harmankaya et al., 2013). The isolated and cross-correlated scattered nP-waves from scatterer 1 for virtual-source location *vs*25 (24 m) are shown in Fig. 15b and d, while the nP-wave results from scatterer 3 for *vs*120 (119 m) are shown in Fig. 15c and e. For the subsequent inversion, we need to use arrivals that are independent of the TBM location, thus only the travel times of cross-correlated scattered waves from Fig. 15d and e are used to obtain the location of scatterers. It should be noted that the interferometric travel-time relation given in Harmankaya et al. (2013) (Eq. 4 below) is valid for point scatterers and single scattering cases. Although there may be scatterers other than point scatterers, the boundaries of the scatterers act as point sources that will allow extraction of information about the scatterer location.

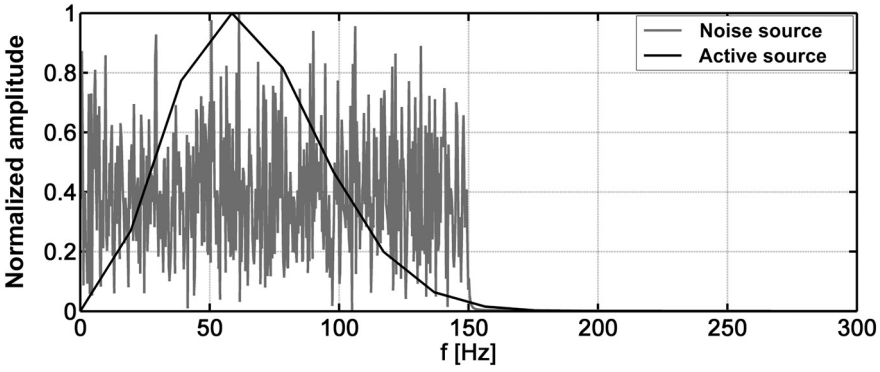

Fig. 10. Amplitude spectrum of the active-source signal (black) and one of the noise-source signals (grey).

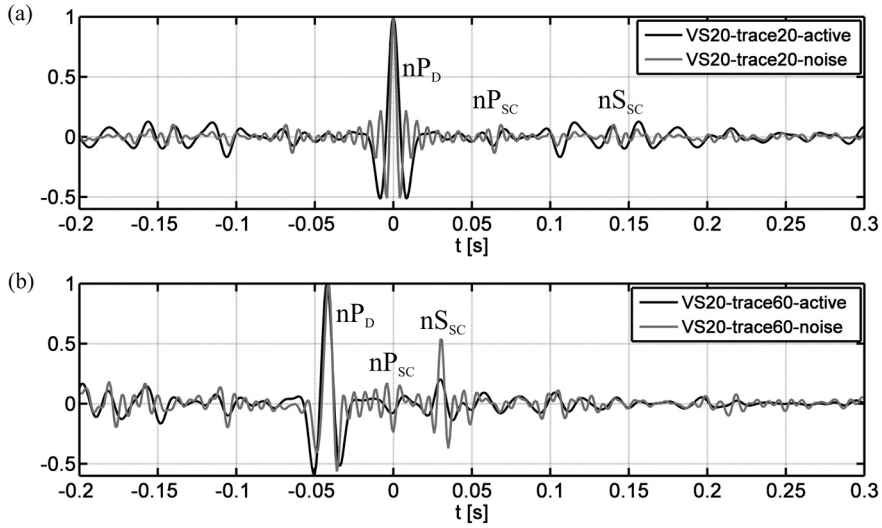

Fig. 11. Comparisons of active- and noise–source correlated traces (a) 20 and (b) 60 from the retrieved results in Fig. 8b and d, respectively.

To estimate the location of a scatterer, the following travel-time relation is used (Harmankaya et al., 2013):

$$t = \frac{1}{V}\left\{ \left[(x_i^r - x)^2 + (z_i^r - z)^2\right]^{1/2} - \left[(x_{vs} - x)^2 + (z_{vs} - z)^2\right]^{1/2} \right\}. \quad (4)$$

The relation calculates non-physical (ghost) traveltimes between the *vs*, the scatterer (point scatterer, as it is defined by a single set of coordinates), and the receivers. In Eq. (4), V is the wave velocity, i is the index for the receiver numbers, r and vs denote the receiver and virtual source, respectively, and x and z are the horizontal and vertical coordinates of a scatterer. The traveltime relation Eq. 4 is used in an inversion to estimate the unknown model parameters (the x and z location of the object) from the observed traveltimes obtained for each *vs* location. The weakly nonlinear problem is solved iteratively by using damped singular value decomposition (SVD). Here, the system of equations for the forward problem is given as $\mathbf{\Delta d} = \mathbf{G}\Delta\mathbf{m}$, where $\mathbf{\Delta d}$ is the difference vector between the observed t_o and the calculated t_c traveltime, $\mathbf{\Delta m}$ is the unknown model parameter vector, and $\mathbf{G}$ is the Jacobian matrix. Rearranging it in SVD terms gives the solution to the inverse problem as

$$\mathbf{\Delta m} = \mathbf{V}\mathbf{\Lambda}\left(\mathbf{\Lambda}^2 + \beta^2\mathbf{I}\right)^{-1}\mathbf{U}^T\mathbf{\Delta d}, \quad (5)$$

where $\mathbf{V}$, $\mathbf{\Lambda}$, $\mathbf{U}$, $\mathbf{I}$ and β are the model-space eigenvectors, the diagonal matrix containing the eigenvalues, the data-space eigenvectors, the identity matrix, and the damping parameter, respectively. The uncertainties of the estimates are obtained by the model covariance matrix using a coverage factor of 2, which provides a confidence level of 95%.

Traveltimes for the inversion are obtained from the non-physical arrivals shown in Fig. 15d and e, by considering the maximum amplitude of these arrivals. As can be observed in Fig. 15a, one side of both scattering hyperbolae are masked and heavily distorted by other arrivals. For the inversion, both sides of a scattering hyperbola need to be defined for correct estimations. As the method assumes a point scatterer, for both scattering hyperbolae undetectable sides are inferred by mirroring the selected sides, though for a limited number of receiver locations. It should be noted that the inversion is done separately for each scatterer.

The results of the inversion for the nP-wave arrivals for both scatterers are given in Fig. 16. In Fig. 16a, the fit between observed (dots) and calculated (lines) traveltimes for each scatterer (*sc1* and *sc3*) are shown. The initial and the updated model parameters – x and z locations of a scatterer – for each iteration are given in Fig. 16b. Initial parameters are selected as $x_0 = 40$ m, $z_0 = 10$ m for the *sc1* inversion and $x_0 = 60$ m, $z_0 = 10$ m for the *sc3* inversion. After six iterations, the locations of the scatterers are estimated accurately. The results are also listed in Table 2. The errors in traveltimes (E_t) are calculated as $E_t = [\sum(t_o - t_c)^2 / \sum (t_c)^2] \times 100$, where t_o and t_c represents observed and calculated traveltimes, respectively. The errors in the model parameters are calculated by $E_m = |(m_a - m_e)/m_a| \times 100$, where m_a and m_e are the actual and estimated model parameters x and z. It should be noted that the error calculations of the model parameters are made relative to the centre point of the scatterers. From the results in Table 2, we can conclude that the locations of the scatterers are estimated with less than 6% error. It is observed here and in the previous studies that in some cases the estimated location parameters correspond to sides/corners of the scatterers. Fig. 17 shows the estimated locations in relation to the actual placement of the scatterers – it can be considered that the locations of the two scatterers are accurately estimated.

Below, we give a summary list of the whole process:

- Obtain a seismic noise record along the TBM path.
- Select a trace to be a virtual source, and correlate it with the other traces; summation of the individual correlation result over the available noise panels. The result is a retrieved common-source gather for a virtual source at the surface at a receiver location.
- Select a scattering hyperbola from the retrieved gather and isolate it from other arrivals using muting.
- Apply only the correlation procedure from step 2 on the isolated scattered arrivals.
- Pick the traveltimes of the retrieved non-physical scattered arrivals after the second correlation.
- Use the traveltimes and appropriate background velocity in the inversion to estimate the location of the object causing the scattered waves.

5. Discussions

We show the applicability of a method similar to the one in Harmankaya et al. (2013) for seismic-noise data due to TBM noise. Only the 2D case is considered here. In other words, the scatterers, TBM, and receivers are located in the same vertical plane. In real life, the problem is likely to have a 3D nature, especially with the receiver-

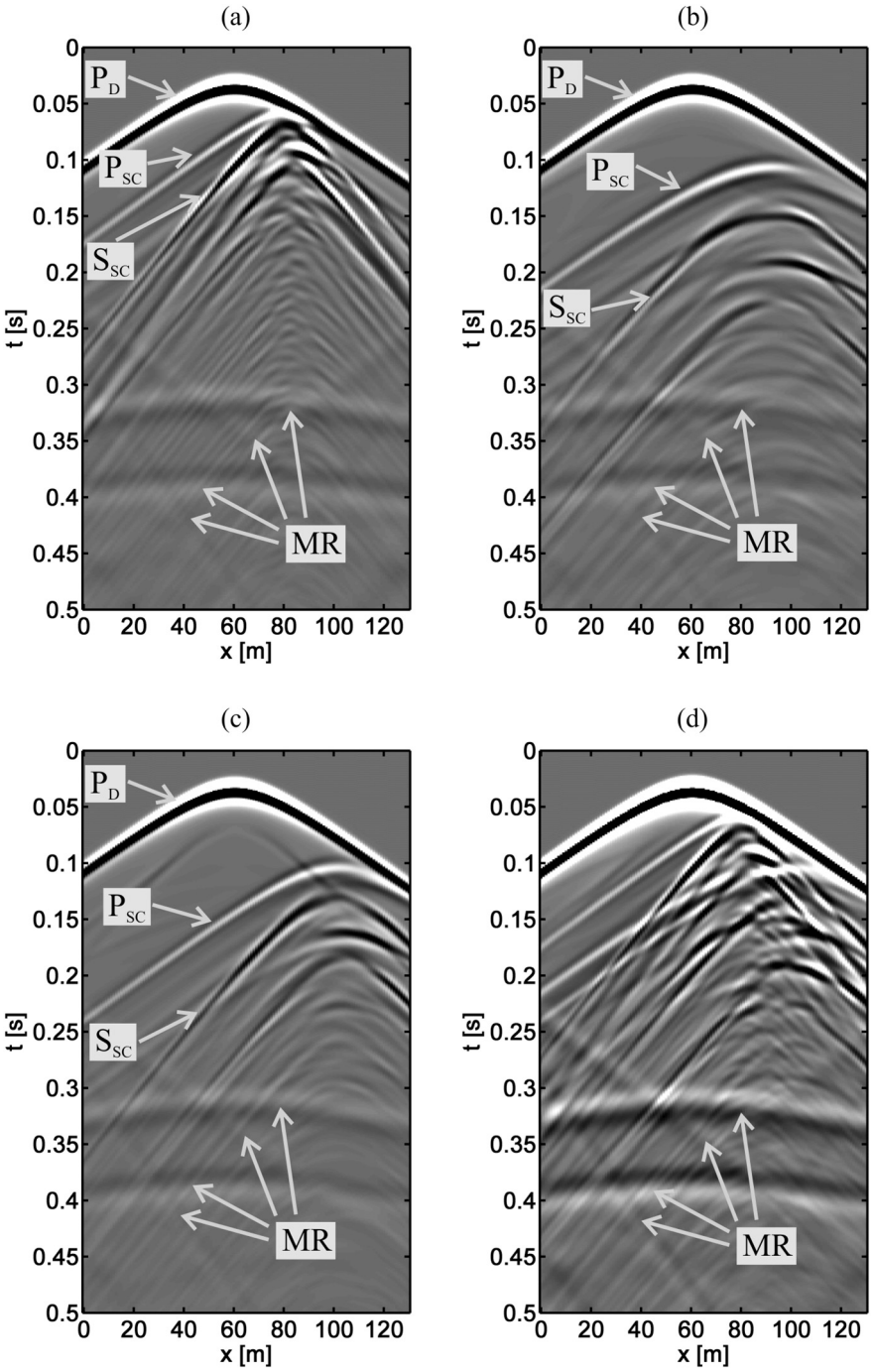

Fig. 12. Active-source modelling results for scatterer (a) *sc1*, (b) *sc2*, and (c) *sc3*. (d) Superposition of the panels a-c. P_D is the direct P-wave arrival, while P_{SC} and S_{SC} are the first scattered P- and S-wave arrivals from a scatterer. MR are the reflections from the bottom and side boundaries of the model. These reflections are present in all the active-source seismograms and consequently present in the correlation panels.

scatterer alignment. As discussed in Kaslilar et al. (2014), 3D application of the method requires at least two receiver lines (parallel or orthogonal) with the same scattered arrivals observed concurrently. For the 3D case, Eq. (4) is slightly modified to incorporate the *y*-location parameter of the scatterer. As each receiver line would produce its own correlation panel, scattered arrivals originating from the same scatterer must be picked out in each panel. In that case, accurate location of scatterer and minimum misfit in traveltime can be obtained. Mismatched arrivals lead to erroneous results in location estimation, as well as relatively large traveltime errors (E_t) (Kaslilar et al., 2014).

In our examples, we consider each cutting blade of the tunneling equipment as an explosive source for simplicity. The type of the source may depend on the model of TBM or on the arrangement of the cutter blades on the cutter head of the TBM. Nevertheless, using a different source type would still result in scattering hyperbolas to which we could apply our method for location estimation.

It is important to note that in this study the TBM is represented as a localized area of noise sources. As the main focus is the objects ahead of the TBM, the excavated tunnel behind the cutter head is not considered in the modelling. This means that any effects that the tunnel would cause are omitted from the resulting seismograms. Such effects would include converted phases of the waves as well as surface waves propagating along tunnel walls and face (Bohlen et al., 2007). Similarly, excavation damage zone around the tunnel is not considered either. All

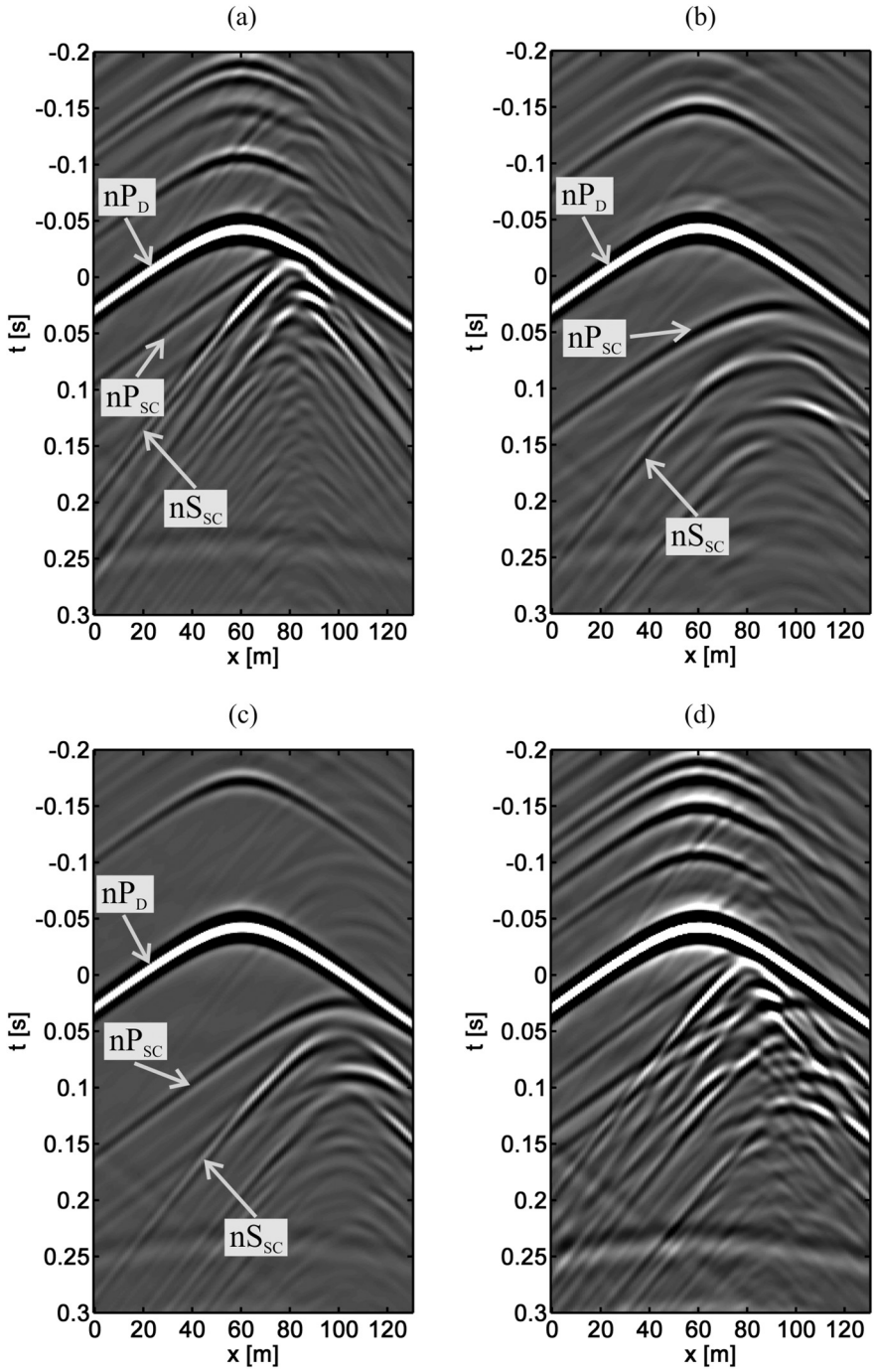

Fig. 13. (a–d) Correlation results using the respective active-source panels from Fig. 12.

these factors would complicate the recorded wavefield even further, thus making it possibly more difficult to pick out the scattered arrivals.

In the modelling, we considered a cavity as a threat in a tunneling process. However, our method is not limited to objects like cavities that are filled with air. If the size of the scatterer is comparable to the seismic wavelength, and if there is contrast in parameters with respect to the background medium in which the scatterer is embedded, then, in case of air (cavity) or a material-filled scatterer (such as boulder or an edge of a fault), we will also be able to locate the scatterer. This would be possible as long as the scattered wavefields are visible and in good shape (not distorted) to select the arrival times for cross-correlations. The differences in the records from a cavity and a material-filled scatterer will be in the polarities of the scattered waveforms.

In the proposed method, we utilize the seismic noise generated by a TBM and recorded at the surface. The noise level of the records at the surface depends on the noise level of the TBM and the properties of the medium. Excavation mode, TBM diameter, and the arrangement of cutter blades are some of the parameters that control the level of the noise-source signal. As the vibrations propagate, the TBM-noise level decreases with distance due to geometrical spreading. In case of soft-ground conditions, intrinsic attenuation will be higher and it will affect the TBM-noise level, as well as the frequency content of the TBM noise. In such a medium, the higher frequencies will be attenuated faster and signal of lower-frequency content will be observed at the surface. As far as the scattering hyperbolas can be observed, the location of the scatterer can still be estimated. As the higher frequencies are attenuated, the waveform will be widened. This may cause some errors in

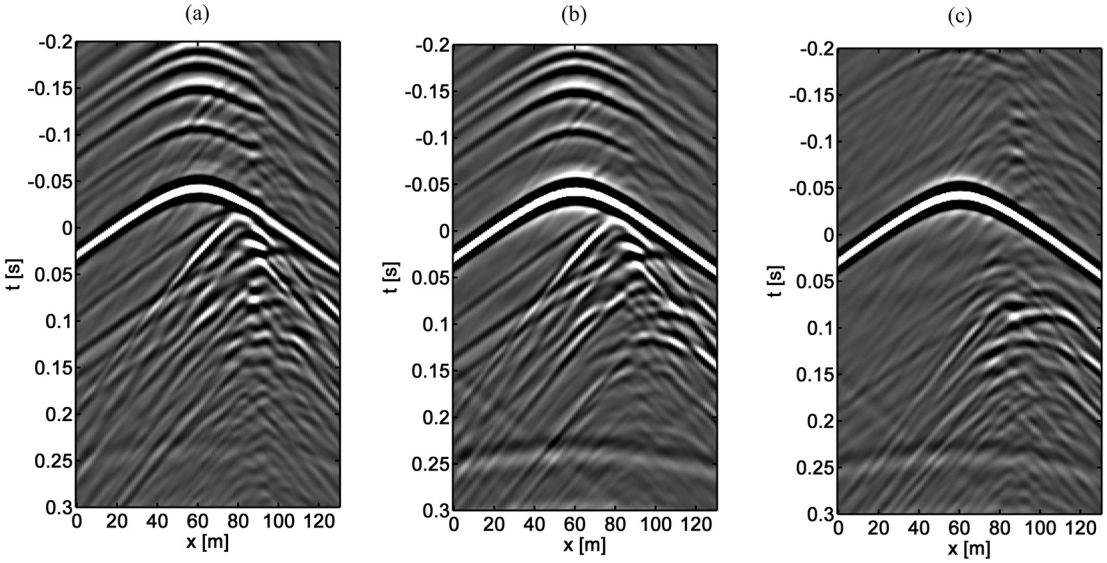

Fig. 14. (a) Correlation panel for modelling all scatterers in Fig. 7 at one time (Fig. 8d repeated). (b) Superposition of correlation panels from single-scatterer modelling (Fig. 13d repeated). (c) Difference of (b) and (a).

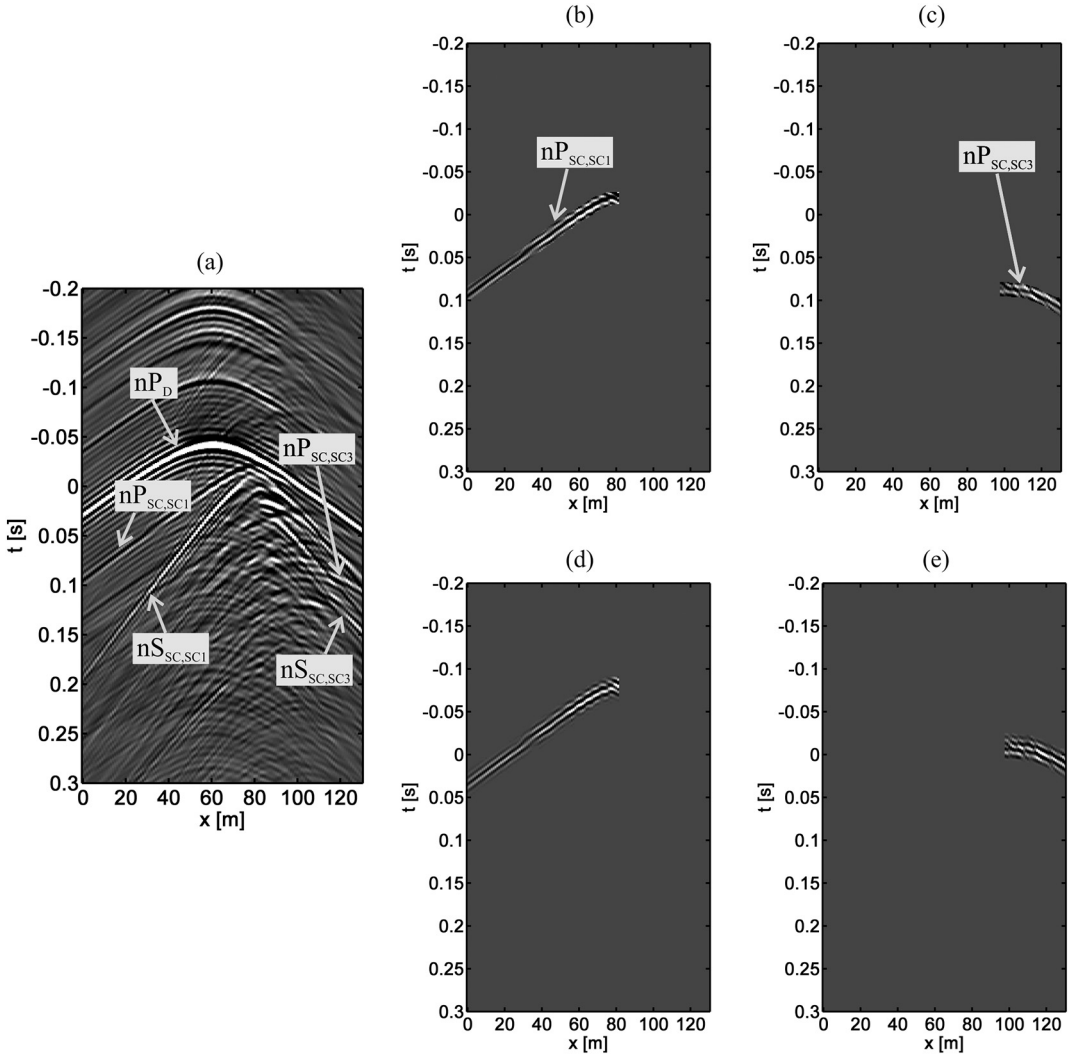

Fig. 15. (a) Correlation result for *vs*20 for the model in Fig. 7. (b) Isolated nP-wave scattered arrivals from scatterer sc1. (c) Isolated nP-wave scattered arrivals from scatterer *sc3*. (d) and (e) Cross-correlation of the nP-wave arrivals given in (b) with the trace at *vs*25 (24 m) and (c) with the trace at *vs*120 (119 m), respectively. nP_{SC} and nS_{SC} are non-physical arrivals due to the scattered P- and S-wave arrivals from the scatterers *sc1* and *sc3*.

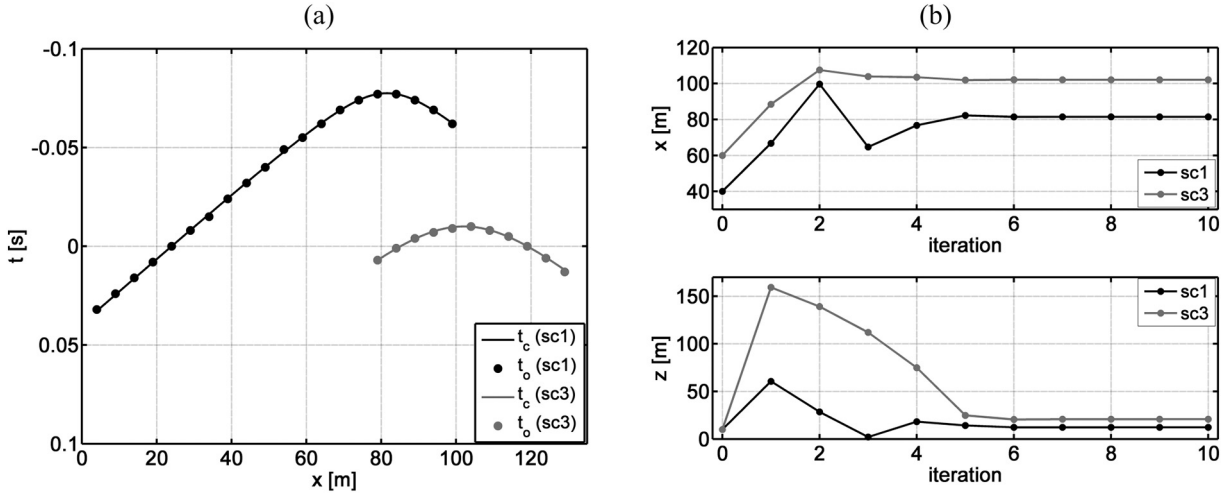

Fig. 16. Inversion results for *sc1* (black) and *sc3* (grey). (a) Observed (dots) and calculated (solid line) traveltimes; (b) Estimated horizontal and vertical locations (*x* and *z*) of the scatterers in each iteration. The values at the zeroth iteration correspond to the initial parameters for the inversion.

the estimations. In such cases, before applying the method we propose, the effect of intrinsic attenuation can be compensated.

After the second cross correlation, the travel paths between the scatterer and the receivers are independent of TBM source positions. In cases where the signal to noise ratio of the scattered arrivals is low, stacking the second cross-correlation panels obtained for different TBM locations could improve the signal to noise ratio. Thus, the selection of the non-physical scattered hyperbola for location purposes will be made easier.

For estimating the location of scatterers, we use Eq. 4. This relation is valid if the medium between the receivers and the scatterers is homogeneous. If there is lateral inhomogeneity between the source and the scatterers, the relation can still be used, as the paths from the source to the scatterers are eliminated (see Harmankaya et al., 2013, Fig. 12 for example). However, if there is inhomogeneity, *e.g.*, layers, between the scatterers and the receivers, Eq. 4 should be adjusted to make use of an effective velocity.

In this paper, for estimating the location of scatterers we utilize scattered P-wave arrivals. If other body- and surface-wave arrivals are detectable and suitable for selecting arrival times, they can also be used for location purposes which may help to reduce the uncertainties in the estimations. As shown above, the success of the method depends on the ability to interpret and select the scattered arrivals. This condition is met for *sc1* and *sc3*, mainly due to the fact that they are the closest and furthest scatterers to the TBM, respectively. Hence, the left side of the scattering hyperbola of *sc1* (closest) and right side of *sc3* (furthest) are observable on the wavefield. As *sc2* is located close to the other two, its scattered arrivals could not be clearly interpreted among the other arrivals. The quality of the estimations suffers from poorly observable arrivals, and as seen in the case of *sc2*, it might even completely prevent any attempt at estimating the location, even though the presence of *sc2* is interpretable in the correlation panels. Nevertheless, one important advantage of our method is its relative ease of use. It does not require any receivers or additional sources on or around the TBM that can interrupt the drilling. Also, compared to borehole drilling, it is cheaper to implement, with the only requirement for receivers at the surface. This makes it practical as a supplementary method to other methods. Detection of other types of heterogeneities, like faults, is also considered for further testing.

Table 2
Estimated model parameters for *sc1* and *sc3* from the configuration given in Fig. 7. The actual location of a scatterer (AL), the estimated model parameters (*x* and *z*) with their 95% confidence levels (1.96 σ), percentage errors on the traveltimes (E_t), and model parameters (E_m) are also given.

	AL (m) x/z	$x \pm \sigma_x$	$z \pm \sigma_z$	E_m (%) x/z	E_t (%)
sc1	82.00/12.00	81.48 ± 0.31	12.30 ± 0.60	0.63/2.50	0.009
sc3	102.00/22.00	102.08 ± 0.23	20.78 ± 1.31	0.08/5.54	0.344

6. Conclusions

We showed the applicability and the potential of a method with noise sources caused by the tunnel boring machine (TBM) while drilling to locate scatterers ahead of the TBM. Our method is inspired by seismic interferometry. We made use of two correlation steps to retrieve non-physical arrivals between the scatterer and receivers at the surface. We then used the retrieved non-physical arrivals to invert their traveltimes to locate the scatterer. We validated our idea using finite-difference simulations of wave propagation. The application of our method to the results from the numerical modelling showed that the location of scatterers can be estimated accurately by using TBM-generated-noise data. The presented method can contribute to drilling

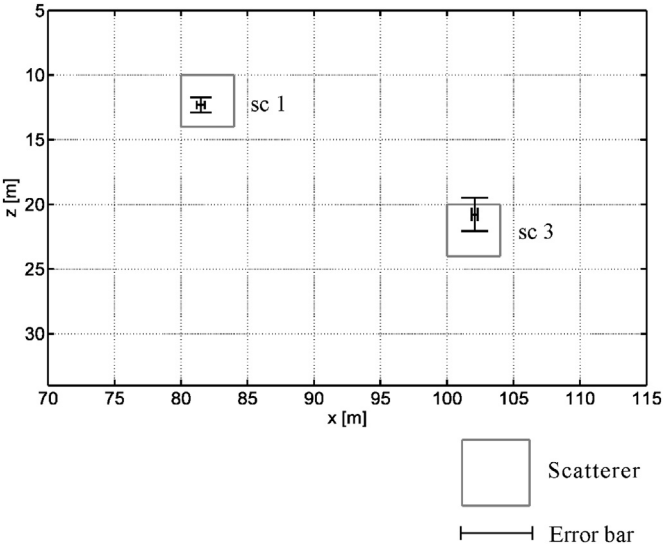

Fig. 17. Estimated location of *sc1* and *sc3* using the TBM noise. Grey squares are the actual scatterers, while the black bars are the horizontal and vertical error bars. The estimated location parameters correspond to the intersection of the error bars.

safety and prevent expensive standstills. Based on the results, it can be said that good estimations can be obtained from scattered arrivals given that they can be reasonably observed after the first correlation step. One important advantage of the method is its relative ease of use while drilling. The presented method is potentially effective for locating scatterers in front of a TBM and can be supplementary to other methods for predicting possible geological threats while tunnel-drilling. We foresee that it can be a useful tool for future tunneling projects.

Acknowledgement

We thank the Editors and two anonymous reviewers for their constructive comments that helped improve the manuscript. The research of D.D. is supported by the Division for Earth and Life Sciences (ALW) with financial aid from the Netherlands Organization for Scientific Research (NWO) with grant VIDI 864.11.009.

References

Ashida, Y., 2001. Seismic imaging ahead of a tunnel face with three-component geophones. Int. J. Rock Mech. Min. Sci. 38, 823–831.

Benecke, N., Dombrowski, B.A., Lehmann, B., 2008. Trust — exploration ahead of the tunnel face for reducing tunneling risks and supporting decision-making. World Tunnel Congress 2008. Underground Facilities for Better Environment and Safety, India, pp. 1124–1129.

Bohlen, T., Lorang, U., Rabbel, W., Müller, C., Giese, R., Lüth, S., Jetschny, S., 2007. Rayleigh-to-shear wave conversion at the tunnel face — from 3D-FD modeling to ahead-of-drill exploration. Geophysics 72, T67–T79.

Brückl, E., Chwatal, W., Dölzlmüller, J., Jöbstl, W., 2001. A study of the application of VSP to exploration ahead of a tunnel. Int. J. Rock Mech. Min. Sci. 38, 833–841.

Brückl, E., Chwatal, W., Mertl, S., Radinger, A., 2008. Exploration ahead of a tunnel face by TSWD - tunnel seismic while drilling. Geomech. Tunnelling 1, 460–465.

Brückl, E., Chwatal, W., Mertl, S., Radinger, A., 2010. Continuous exploration ahead of the tunnel face by TSWD - Tunnel seismic while drilling. Symposium on the Application of Geophysics to Engineering and Environmental Problems 2010, Keystone, Colorado: pp. 353–360 https://doi.org/10.4133/1.3445455.

Dickmann, T., Sander, B., 1996. Drivage concurrent tunnel seismic prediction. Felsbau-Rock and Soil Engineering. 14, pp. 406–411.

Harmankaya, U., Kaslilar, A., Thorbecke, J., Wapenaar, K., Draganov, D., 2013. Locating near-surface scatterers using non-physical scattered waves resulting from seismic interferometry. J. Appl. Geophys. 91, 66–81.

Harmankaya, U., Kaslilar, A., Wapenaar, K., Draganov, D., 2016. Locating scatterers ahead of a tunnel boring machine using noise correlation. 78th EAGE Conference and Exhibition, Vienna, Austria, Extended Abstracts, Tu LHR5 16 https://doi.org/10.3997/2214-4609.201600630.

Hauser, E.C., 2001. Detection and location of obstructions ahead of a tunnel boring machine using the tunneling vibrations as a seismic source – the first successful example. Symposium on the Application of Geophysics to Engineering and Environmental Problems. 2001 (pp. SSI7-SSI7).

Jetschny, S., Bohlen, T., Kurzmann, A., 2011. Seismic prediction of geological structures ahead of the tunnel using tunnel surface waves. Geophys. Prospect. 59, 934–946.

Jiao, Y.Y., Tian, H.N., Liu, Y.Z., Mei, R.W., Li, H.B., 2015. Prediction of tunneling hazardous geological zones using the active seismic approach. Near Surf. Geophys. 13, 333–342.

Kaslilar, A., Harmankaya, U., Wapenaar, K., Draganov, D., 2013. Estimating the location of a tunnel using correlation and inversion of Rayleigh wave scattering. Geophys. Res. Lett. 40, 6084–6088.

Kaslilar, A., Harmankaya, U., Van Wijk, K., Wapenaar, K., Draganov, D., 2014. Estimating location of scatterers using seismic interferometry of scattered rayleigh waves. Near Surf. Geophys. 12, 721–730.

Kaus, A., Boening, W., 2008. BEAM – geoelectrical ahead monitoring for TBM-drives. Geomech. Tunn. 1, 442–449.

Kneib, G., Kassel, A., Lorenz, K., 2000. Automatic seismic prediction ahead of the tunnel boring machine. First Break 18, 295–302.

Kopp, T., 2012. Real-time monitoring of geological conditions during mechanized tunneling by means of BEAM4 method. Proceedings of the 1st Eastern European Tunneling Conference, Budapest, Hungary.

Li, S., Sun, H., Lu, X., Li, X., 2014. Three-dimensional modeling of transient electromagnetic responses of water-bearing structures in front of a tunnel face. J. Environ. Eng. Geophys. 19, 13–32.

Meles, A.G., Curtis, A., 2013. Physical and non-physical energy in scattered wave source-receiver interferometry. J. Acoust. Soc. Am. 133, 3790–3801.

Musayev, K., Oezalp, S., Hackl, K., Baitsch, M., 2016a. Full acoustic waveform inversion in a pml-truncated tunnel environment. 15th EAGE International Conference on Geoinformatics – Theoretical and Applied Aspects, Kiev, Ukraine https://doi.org/10.3997/2214-4609.201600551.

Musayev, K., Lamert, A., Hackl, K., Friederich, W., Baitsch, M., 2016b. Predicting the geological structure ahead of a tunnel using full waveform inversion – a blind test. 78th EAGE Conference and Exhibition, Vienna, Austria, Extended Abstracts, Tu SBT4 09 https://doi.org/10.3997/2214-4609.201600793.

Nyugen, L.T., Nestorovic, T., 2016. Advance exploration by stochastic inversion of tunnel seismic waves - a numerical study. World Tunnel Congress 2016, San Francisco, USA.

Petronio, L., Poletto, F., 2002. Seismic-while-drilling by using tunnel boring machine noise. Geophysics 67, 1798–1809.

Petronio, L., Poletto, F., Schleifer, A., 2007. Interface prediction ahead of the excavation front by the tunnel-seismic-while-drilling (TSWD) method. Geophysics 72, G39–G44.

Poletto, F., Petronio, L., 2006. Seismic interferometry with a TBM source of transmitted and reflected waves. Geophysics 71, SI85–SI93.

Sattel, G., Frey, P., Amberg, R., 1992. Prediction ahead of the tunnel face by seismic methods - pilot project in Centovalli Tunnel, Locarno, Switzerland. First Break 10, 19–25.

Sattel, G., Sander, B.K., Amberg, F., Kashiwa, T., 1996. Predicting ahead of the face–tunnel seismic prediction. Tunn. Tunn. Int. 28, 24–30.

Schaeffer, K., Mooney, M.A., 2016. Examining the influence of TBM-ground interaction on electrical resistivity imaging ahead of the TBM. Tunn. Undergr. Sp. Technol. 58, 82–98.

Snieder, R., Fleury, C., 2010. Cancellation of spurious arrivals in Green's function retrieval of multiple scattered waves. J. Acoust. Soc. Am. 128, 1598–1605.

Snieder, R., Wapenaar, K., Larner, K., 2006. Spurious multiples in seismic interferometry of primaries. Geophysics 71, SI111–SI124.

Snieder, R., Van Wijk, K., Haney, M., Calvert, R., 2008. Cancellation of spurious arrivals in Green's function extraction and the generalized optical theorem. Phys. Rev. E 78, 036606.

Swinnen, G., Thorbecke, J.W., Drijkoningen, G.G., 2007. Seismic imaging from a TBM. Rock Mech. Rock. Eng. 40, 577–590.

Thorbecke, J.W., Draganov, D., 2011. Finite-difference modeling experiments for seismic interferometry. Geophysics 76, H1–H18.

Wapenaar, K., Draganov, D., Snieder, R., Campman, X., Verdel, A., 2010. Tutorial on seismic interferometry: part 1 – basic principles and applications. Geophysics 75 (75A195–75A209).

Xue, G.Q., Yan, Y.J., Li, X., Di, Q.Y., 2007. Transient electromagnetic S-inversion in tunnel prediction. Geophys. Res. Lett. 34, L18403.

Zhao, Y., Jiang, H., Zhao, X., 2006. Tunnel seismic tomography method for geological prediction and its application. Appl. Geophys. 3, 69–74.